

RESEARCH ARTICLE | OCTOBER 17 2023

Plasmon-enhanced circular dichroism spectroscopy of chiral drug solutions

Special Collection: [Chirality of Plasmonic Structures and Materials](#)

Matteo Venturi ; Raju Adhikary; Ambaresh Sahoo; Carino Ferrante ; Isabella Daidone ; Francesco Di Stasio ; Andrea Toma ; Francesco Tani ; Hatice Altug; Antonio Mecozzi ; Massimiliano Aschi ; Andrea Marini  

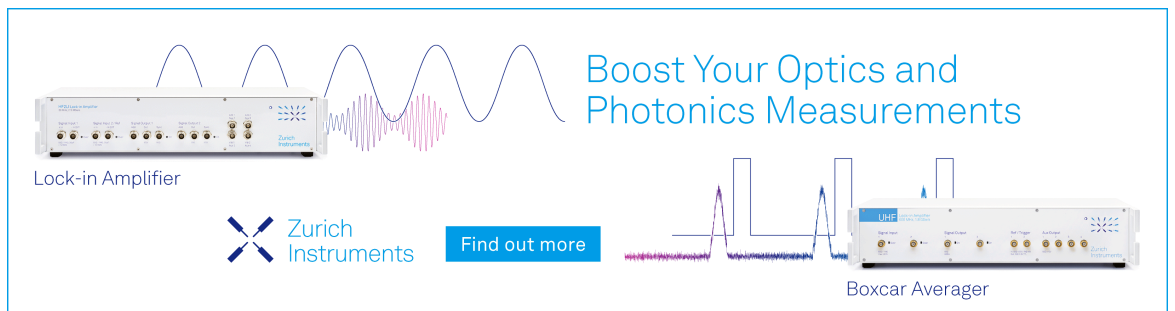


J. Chem. Phys. 159, 154703 (2023)

<https://doi.org/10.1063/5.0169826>



CrossMark



Boost Your Optics and Photonics Measurements

Lock-in Amplifier

Zurich Instruments

Find out more

Boxcar Averager

Plasmon-enhanced circular dichroism spectroscopy of chiral drug solutions

Cite as: *J. Chem. Phys.* **159**, 154703 (2023); doi: [10.1063/5.0169826](https://doi.org/10.1063/5.0169826)

Submitted: 28 July 2023 • Accepted: 1 October 2023 •

Published Online: 17 October 2023



View Online



Export Citation



CrossMark

Matteo Venturi,¹  Raju Adhikary,¹ Ambaresh Sahoo,¹ Carino Ferrante,²  Isabella Daidone,¹ 
Francesco Di Stasio,³  Andrea Toma,³  Francesco Tani,⁴  Hatice Altug,⁵  Antonio Mecozzi,¹ 
Massimiliano Aschi,¹  and Andrea Marini^{1,2,a)} 

AFFILIATIONS

¹ Department of Physical and Chemical Sciences, University of L'Aquila, Via Vetoio, 67100 L'Aquila, Italy

² CNR-SPIN, c/o Dip.to di Scienze Fisiche e Chimiche, Via Vetoio, Coppito (L'Aquila) 67100, Italy

³ Istituto Italiano di Tecnologia, Via Morego 30, Genova 16136, Italy

⁴ Max Planck Institute for the Science of Light, Staudtstr. 2, 91058 Erlangen, Germany

⁵ Institute of Bioengineering, Ecole Polytechnique Federale de Lausanne (EPFL), Lausanne 1015, Switzerland

Note: This paper is part of the JCP Special Topic on Chirality of Plasmonic Structures and Materials.

Author to whom correspondence should be addressed: andrea.marini@univaq.it

ABSTRACT

We investigate the potential of surface plasmon polaritons at noble metal interfaces for surface-enhanced chiroptical sensing of dilute chiral drug solutions with nl volume. The high quality factor of surface plasmon resonances in both Otto and Kretschmann configurations enables the enhancement of circular dichroism differential absorption thanks to the large near-field intensity of such plasmonic excitations. Furthermore, the subwavelength confinement of surface plasmon polaritons is key to attain chiroptical sensitivity to small amounts of drug volumes placed around ≈ 100 nm by the metal surface. Our calculations focus on reparixin, a pharmaceutical molecule currently used in clinical studies for patients with community-acquired pneumonia, including COVID-19 and acute respiratory distress syndrome. Considering realistic dilute solutions of reparixin dissolved in water with concentration ≤ 5 mg/ml and nl volume, we find a circular-dichroism differential absorption enhancement factor of the order ≈ 20 and chirality-induced polarization distortion upon surface plasmon polariton excitation. Our results are relevant for the development of innovative chiroptical sensors capable of measuring the enantiomeric imbalance of chiral drug solutions with nl volume.

© 2023 Author(s). All article content, except where otherwise noted, is licensed under a Creative Commons Attribution (CC BY) license (<http://creativecommons.org/licenses/by/4.0/>). <https://doi.org/10.1063/5.0169826>

I. INTRODUCTION

Chiral sensing plays a key role in pharmaceuticals because the specific enantiomeric form of drugs affects their functionality and toxicity.¹ Current state-of-the-art techniques capable of measuring enantiomeric excess of chiral mixtures, e.g., nuclear magnetic resonance,² gas chromatography³ and high performance liquid chromatography,⁴ provide advanced tools for drug safety, but are designed to operate with macroscopic drug volumes and are not suitable for real-time analysis and innovative lab-on-a-chip integration schemes. Photonic devices can potentially overcome such limitations, but technological advancement in this direction is hampered by the inherently weak chiroptical interaction, which

requires ml volumes in order to attain sensitivity to the enantiomeric imbalance of chiral drug solutions through, e.g., polarimetry⁵ or electronic/vibrational circular dichroism (CD).^{6,7} Diverse approaches are currently investigated to enhance chiroptical interaction, as in particular ultrafast and nonlinear chiroptical spectroscopy techniques^{8–11} or the exploitation of superchiral fields^{12,13} that can be engineered via metasurfaces and nanophotonic structures.^{14–16} However, the actual exploitation of superchiral fields for novel chiral sensing schemes remains elusive, mainly because most of the experimental sensing demonstrations in literature rely on chiral nanoplasmonic substrates. The major issue is that when a chiral sample is placed in the near-field of such nanostructures, the detected CD signal is contaminated by the chiroptical response of the

nanostructure itself, which acts as a strong background noise and masks the weak chiroptical signal of the actual sample.¹⁷ It has to be noted that chiral drugs diluted in solutions are continuously deformed by the conformational fluctuations of the molecule in interaction with the solvent at finite temperature, modulating over time their chiroptical response. Concurring electric and magnetic resonances in nanostructures provide enhanced CD thanks to the dual enhancement of both electric and magnetic fields.¹⁸ While such schemes are promising for single molecule chiral discrimination, they are difficult to implement for extended drug solutions because CD enhancement is attained only at specific hot spots where electric and magnetic field lines are strong, parallel and $\pi/2$ shifted.^{17,18} Over a complementary direction, metal-based nanophotonic structures enable plasmon-enhanced CD spectroscopy,¹⁹ which has been predicted for isolated molecules,²⁰ while it has been adopted mainly to characterise chiral nanoparticles.^{21–23}

Here we predict that CD differential absorption (CDDA) by nl volumes of dilute drug solutions can get enhanced by a

factor $f_{\text{CDDA}} \approx 20$ via the excitation of surface plasmon polaritons (SPPs) at a planar interface between a noble metal and the chiral sample. In particular, we focus on an isotropic assembly of reparixin (an inhibitor of the CXCR2 function attenuating inflammatory responses²⁴ that has been adopted in clinical trials for the treatment of hospitalized patients with COVID-19 pneumonia²⁵) dissolved in water with dilute number molecular density of the order $n_{\text{mol}} = n_{\text{mol}}^{\text{R}} + n_{\text{mol}}^{\text{S}} \approx 10^{-2} \text{ nm}^{-3}$ (corresponding to a concentration of 5 mg/ml), where $n_{\text{mol}}^{\text{R,S}}$ indicate the number densities of R and S enantiomers, respectively. Because SPPs possess a momentum greater than the one of radiation in vacuum, their excitation requires a radiation momentum kick, which can be provided either by a grating^{26,27} or by a prism through attenuated total reflection in Kretschmann²⁸ or Otto²⁹ configurations. However, the adoption of gratings to excite SPPs modifies significantly the SPP dispersion,³⁰ and in turn here we focus on silica prism coupling. We observe that CDDA $\Delta A = A_{\text{R}} - A_{\text{L}}$ upon right/left circular polarization excitation is proportional to the enantiomeric excess density

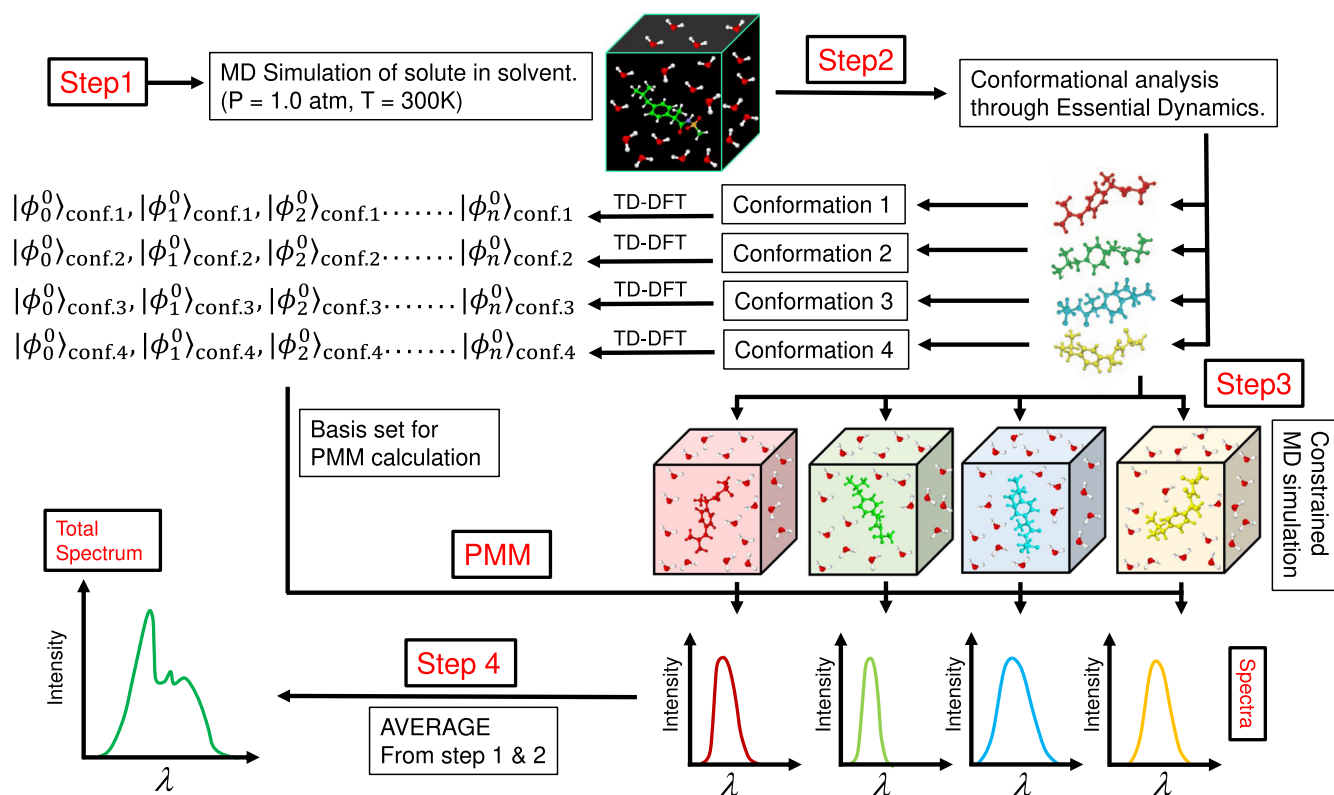


FIG. 1. **Step 1.** MD simulation of reparixin in water. **Step 2.** (2a) Conformational analysis of the trajectory from **Step 1** through Essential Dynamics (see supplementary material). (2b) Extraction of the (four) reparixin conformation states, representative of high-probability basins (see, Fig. 2), for TD-DFT calculations (in the gas-phase) aimed at obtaining the unperturbed basis-set, of size N_s , necessary for **Step 3** (c). **Step 3.** (3a) For each reparixin conformation state a further MD simulation is carried out with solute kept frozen and the solvent allowed to move. (3b) The electric field exerted by the solvent is evaluated onto the reparixin center of mass at each frame of the trajectory of the previous section. (3c) The basis set obtained in the **Step 2** (b) and the electric field from the **Step 3** (b) Perturbed Matrix Method (see supplementary material) is applied for evaluating, at each frame of the trajectory of **Step 3** (a), the instantaneous expectation value of interest (electric dipole, electronic energy, vibrational energy) or the instantaneous values of electric or magnetic transition moment. The latter are used to obtain the UV and/or CD spectrum, either electronic or vibrational. **Step 4.** According to the probability of conformation state basins, all the above observables (including the spectra), the observables - assuming an ergodic behaviour of the produced trajectories - are calculated as time-averages and represent ensemble averages.

$\Delta n_{\text{mol}} = n_{\text{mol}}^{\text{S}} - n_{\text{mol}}^{\text{R}}$, and in turn by measuring the CDDA it is possible to retrieve Δn_{mol} . Furthermore, we observe that the maximum plasmon-induced CDDA enhancement factor $f_{\text{CDDA}} \approx 20$ is attained with silver in the Otto configuration, while other noble metals like gold and copper provide a smaller f_{CDDA} . The vacuum wavelength (λ) dependence of all macroscopic optical parameters [dielectric permittivity $\epsilon_r(\lambda)$, magnetic permeability $\mu_r(\lambda)$ and chiral parameter $\kappa(\lambda)$] of the isotropic chiral mixture are calculated from first principles. This is accomplished by perturbatively solving the density matrix equations accounting for the leading electronic and vibrational absorption peaks and by averaging the obtained polarizability tensors over the random molecular orientation through the Euler rotaton matrix approach.^{31,32} We evaluate plasmon-enhanced CDDA ΔA by classical electrodynamics calculations accounting for (i) silica prism in the Otto and Kretschmann SPP coupling schemes, (ii) the macroscopic bi-anisotropic response of the chiral mixture, and (iii) the dielectric response of noble metals. Our predictions of efficient plasmon-enhanced CDDA by isotropic drug solutions of nl volume suggest novel avenues for integrated chiroptical sensing.

For the present study, it is necessary to make use of quantum molecular observables (i.e., electric and magnetic moments, electronic and vibrational excitation energies) evaluated for the solvated drug, i.e., aqueous reparixin in our calculations. This is not a trivial task because such quantum molecular observables should be perceived as genuinely quantum expectation values averaged (in statistical-mechanical terms) over a large number of reparixin/solvent configurations. For this purpose we have adopted a combination of computational approaches, described to some extent in the supplementary material and briefly illustrated in Fig. 1. The adopted methods combine semi-classical Molecular Dynamics (MD) simulations (necessary for the reparixin-solvent conformational sampling), quantum-chemical (QM) calculations and Perturbed Matrix Method (PMM)^{33–35} which, using the information obtained from MD simulations and QM calculations, provides the observables of interests expressed as ensemble averages. This approach is necessary for including in our model subtle but relevant

effects produced by the semi-classical atomic-molecular motions (both reparixin and water).

II. ELECTRONIC AND VIBRATIONAL STRUCTURE OF REPARIXIN IN WATER

In Figs. 2(a)–2(c) we illustrate in more detail the key-steps for evaluating the quantum-molecular observables of interest. As previously described in Fig. 1 and in the supplementary material, the reparixin electric/magnetic transition dipole moments and the corresponding absorption UV/vibrational spectra are evaluated as ensemble averages of solvated reparixin in water. These high probability conformation states are representative of the free-energy basins b_k , where $k = 1 - 4$, located through MD simulations and ED analysis and depicted in Fig. 2 in the case of reparixin S enantiomer. We underline that, due to selection rules, we consider only two vibrational states (labelled by the index $\nu = 0, 1$) producing resonant interaction with external radiation in the mid-infrared (mid-IR) with vibrational energy $\hbar\omega_\nu$ independent over the reparixin conformation state k . Indeed, we found that $\hbar\omega_\nu$ is practically unaffected by the molecular configuration state, i.e., the nature of the vibrational mode (calculated as described in the supplementary material) coincides in the four conformation states. For every enantiomer labelled by the index $a = \text{R, S}$, the radiation-unperturbed vibronic structure is approximated by independent electronic/vibrational Hamiltonians $\hat{\mathcal{H}}_0^{\text{el,vib}}(k, a)$, given by

$$\hat{\mathcal{H}}_0^{\text{el}}(k, a) = \sum_{i=1}^5 \hbar\omega_i(k) |i(k, a)\rangle \langle i(k, a)|, \quad (1a)$$

$$\hat{\mathcal{H}}_0^{\text{vib}}(a) = \sum_{\nu=0,1} (\nu + 1/2) \hbar\omega_\nu | \nu(a) \rangle \langle \nu(a) |, \quad (1b)$$

where $\hbar\omega_i(k)$ and $\hbar\omega_\nu(\nu + 1/2)$ are the electronic/vibrational energy eigenvalues with eigenstates $|i(k, a)\rangle$ and $|\nu(a)\rangle$. For flexible solvated molecules such as reparixin, the effect of the vibronic transitions in the UV spectral shape is negligible if compared to the one produced by the chromophore and solvent conformational transitions.

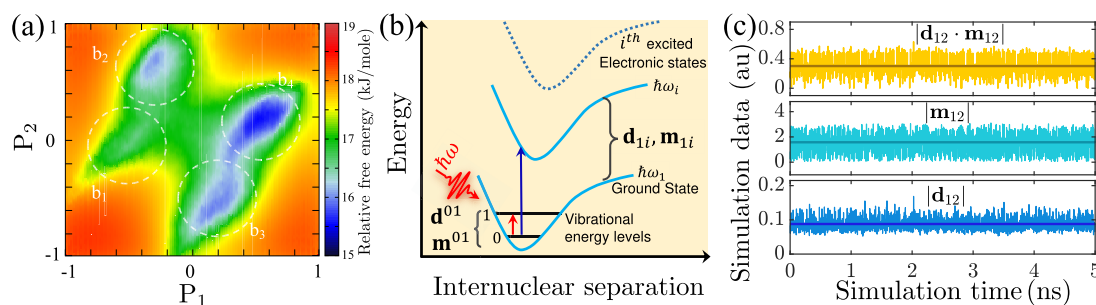


FIG. 2. (a) Calculated relative free-energy at $T = 298$ K of the reparixin pure S enantiomer (dissolved in water) through MD simulations followed by Essential Dynamics analysis (see supplementary material for details), indicating the co-existence of four distinct, statistically relevant conformation state basins b_k , where $k = 1 - 4$. P_1 and P_2 represent the projections of the solvated reparixin position vectors (sampled during the MD simulation) onto the eigenvectors of the all-atoms covariance matrix (see supplementary material for additional details). (b) Sketch of reparixin vibronic dynamics produced by a driving optical laser field in the electric/magnetic dipole approximation. (c) Temporal evolution of electronic transition dipole moduli $|\mathbf{d}_{1,2}|$, $|\mathbf{m}_{1,2}|$, and chiral projection $|\mathbf{d}_{1,2} \cdot \mathbf{m}_{1,2}|$ (in atomic units) of a single reparixin molecule in the b_1 conformation state calculated at each temporal frame (expressed in nanoseconds) of the MD simulation through PMM calculations (see supplementary material for additional details). We emphasize that the MD simulation box size is ≈ 3 nm lateral size and ≈ 27 nm³ volume, and is unrelated to the 100 nm thickness of the chiral sample used.

In turn, the lack of fine structure in the electronic transitions is due to the effect of the semi-classical molecular vibrations and solvent perturbations producing a spectral broadening that prevents their observation. Furthermore, we account only for the electronic states $i = 1 - 5$ because we find that the corresponding energy levels are the only ones producing resonant electronic absorption peaks in the ultraviolet (UV). Figure 2(b) illustrates the schematic vibronic structure of reparixin for a generic molecular conformation state. In the electric/magnetic dipole approximation, the molecule interacts with external radiation through the electronic/vibrational perturbing Hamiltonians given by the expressions

$$\hat{\mathcal{H}}_{\text{I,el}}^{(k,a)}(\mathbf{r}, t) = -\mathbf{E}(\mathbf{r}, t) \cdot \hat{\mathbf{d}}_{\text{el}}(k, a) - \mathbf{B}(\mathbf{r}, t) \cdot \hat{\mathbf{m}}_{\text{el}}(k, a), \quad (2a)$$

$$\hat{\mathcal{H}}_{\text{I,vib}}^{(a)}(\mathbf{r}, t) = -\mathbf{E}(\mathbf{r}, t) \cdot \hat{\mathbf{d}}_{\text{vib}}(a) - \mathbf{B}(\mathbf{r}, t) \cdot \hat{\mathbf{m}}_{\text{vib}}(a), \quad (2b)$$

where $\mathbf{E}(\mathbf{r}, t)$, $\mathbf{B}(\mathbf{r}, t)$ are the external radiation electric and magnetic induction fields and

$$\hat{\mathbf{d}}_{\text{el}}(k, a) = \sum_{i,j=1}^5 \mathbf{d}_{i,j}(k, a) |i(k, a)\rangle \langle j(k, a)|, \quad (3a)$$

$$\hat{\mathbf{m}}_{\text{el}}(k, a) = \sum_{i,j=1}^5 \mathbf{m}_{i,j}(k, a) |i(k, a)\rangle \langle j(k, a)|, \quad (3b)$$

$$\hat{\mathbf{d}}_{\text{vib}}(a) = \sum_{v,v'=0,1} \mathbf{d}^{v,v'}(a) |v(a)\rangle \langle v'(a)|, \quad (3c)$$

$$\hat{\mathbf{m}}_{\text{vib}}(a) = \sum_{v,v'=0,1} \mathbf{m}^{v,v'}(a) |v(a)\rangle \langle v'(a)| \quad (3d)$$

indicate the dyadic representation of electric/magnetic electronic/vibrational dipole operators in the set of radiation-unperturbed electronic/vibrational energy states. We emphasize that, for the particular case of reparixin, due to the co-presence of two electrons with opposite spins in the ground state, the static magnetic dipole moments are vanishing for every electron eigenstate (in the Born-Oppenheimer approximation), while static electric dipole moments are finite. In turn, the calculation of vibrational magnetic transition dipole moments \mathbf{m}^{01} requires going beyond the Born-Oppenheimer approximation, see supplementary material for additional details. Note that transition electric dipole moments are real polar vectors $\mathbf{u}(k, a) \in \mathfrak{R}^3$, while transition magnetic dipole moments are purely imaginary axial vectors $\mathbf{w}(k, a) \in \mathfrak{S}^3$, where we indicate with $\mathbf{u}(k, a)$ either $\mathbf{d}_{1i}(k, a)$ or $\mathbf{d}^{01}(a)$, and with $\mathbf{w}(k, a)$ either $\mathbf{m}_{1i}(k, a)$ or $\mathbf{m}^{01}(a)$, depending over the electronic/vibrational dynamics considered. We define the reflection operator $\mathcal{R}_{\hat{\mathbf{n}}} = \mathbb{I} - 2\hat{\mathbf{n}}\hat{\mathbf{n}}$ by the plane perpendicular to the unit vector $\hat{\mathbf{n}}$ where reflection symmetry is broken. Transition dipole moments of opposite enantiomers can be calculated by applying the reflection operator: $\mathbf{u}(k, S) = \mathcal{R}_{\hat{\mathbf{n}}}\mathbf{u}(k, R)$, $\mathbf{w}(k, S) = -\mathcal{R}_{\hat{\mathbf{n}}}\mathbf{w}(k, R)$. In turn, while the modulus of the transition dipole moments is unaffected by the enantiomeric type $|\mathbf{u}(k, S)| = |\mathbf{u}(k, R)|$, $|\mathbf{w}(k, S)| = |\mathbf{w}(k, R)|$, the scalar product $\mathbf{u}(k, S) \cdot \mathbf{w}(k, S) = -\mathbf{u}(k, R) \cdot \mathbf{w}(k, R)$ flips sign for opposite enantiomeric forms. Such a quantity, which we call *chiral projection*, is in turn chirally sensitive as it involves the scalar product of a polar and an axial vector. In Fig. 2(c) we report the MD-induced temporal evolution of electronic contributions $|\mathbf{d}_{12}|$, $|\mathbf{m}_{12}|$ and the modulus of the chiral projection $|\mathbf{d}_{12} \cdot \mathbf{m}_{12}|$ of the S reparixin enantiomer in conformation state $k = 1$. Note that such

quantities, constituting the key microscopic ingredients producing optical activity, see below, depend over time due to MD. For this reason, in our quantum-mechanical calculations of the macroscopic bi-anisotropic response we use ensemble-averaged $\langle |\mathbf{d}_{12}| \rangle$, $\langle |\mathbf{m}_{12}| \rangle$ and $\langle |\mathbf{d}_{12} \cdot \mathbf{m}_{12}| \rangle$ (calculated as time-averages over the \approx ns MD timescale in our ergodic assumption, see below).

III. MACROSCOPIC BI-ANISOTROPIC RESPONSE OF REPARIXIN IN WATER

For every conformation state k and enantiomeric form a , radiation-induced electron/vibrational dynamics of chiral drugs (reparixin in our calculations) is in turn governed by the density matrix equations

$$\frac{d\hat{\rho}_{k,a}}{dt} = \frac{1}{i\hbar} \left[\hat{\mathcal{H}}_0^{\text{el,vib}}(k, a) + \hat{\mathcal{H}}_{\text{I,el,vib}}^{(k,a)} \hat{\rho}_{k,a} \right] + \hat{\mathcal{L}}(\hat{\rho}_{k,a}), \quad (4)$$

where $\hat{\rho}_{k,a} = \hat{\rho}_{k,a}^{\text{el,vib}}(\mathbf{r}, t)$ is the time-dependent electronic/vibrational density matrix and $\hat{\mathcal{L}}(\hat{\rho}_{k,a}^{\text{el,vib}})$ is the Lindblad operator accounting for interaction with the thermal bath. The Lindblad relaxation rates are obtained by fitting the bandwidth of the absorption spectra, see supplementary material for further details. For monochromatic external radiation fields $\mathbf{V}(\mathbf{r}, t) = \text{Re}[\mathbf{V}_0(\mathbf{r})e^{-i\omega t}]$ with carrier vacuum wavelength $\lambda = 2\pi c/\omega$, where c is the speed of light in vacuum and $\mathbf{V} = \mathbf{E}, \mathbf{B}$, respectively, Eq. (4) is solved perturbatively at first-order yielding $\hat{\rho}_{k,a}^{\text{el,vib}}(\mathbf{r}, t)$.³⁶ The expectation value of the induced electric/magnetic dipole moments expressed as an ensemble average considering all the reparixin conformation states for each enantiomer form a (see Fig. 1), is in turn given by $\mathbf{o}_a^{\text{el,vib}} = \sum_{k=1}^4 p(k) \text{Tr}[\hat{\rho}_{k,a}^{\text{el,vib}} \hat{\mathbf{o}}(k, a)]$, where $p(k) = 0.25$, see Fig. 2(a), and $\mathbf{o} = \mathbf{d}, \mathbf{m}$, respectively. Owing to the random molecular orientation, the induced electric/magnetic dipole moments averaged over arbitrary rotations through the Euler rotation matrix approach^{31,32} are given by the expressions

$$\langle \mathbf{d}_a \rangle = \varepsilon_0 \text{Re} \left\{ \left[\alpha_e \mathbf{E}_0 + c\alpha_m^{(a)} \mathbf{B}_0 \right] e^{-i\omega t} \right\}, \quad (5a)$$

$$\langle \mathbf{m}_a \rangle = \varepsilon_0 c \text{Re} \left\{ \left[-\alpha_m^{(a)} \mathbf{E}_0 + c\alpha_b \mathbf{B}_0 \right] e^{-i\omega t} \right\}, \quad (5b)$$

where ε_0, μ_0 are the vacuum permittivity and permeability, respectively, and $\alpha_e(\omega), \alpha_b(\omega), \alpha_m^{(a)}(\omega)$ are the linear isotropic electric, magnetic and mixing polarizabilities of every molecular enantiomer, given by the expressions

$$\alpha_{e,b,m}^{(a)}(\omega) = C_{e,b,m}^{(\text{vib})}(a) \mathcal{F}^{(\text{vib})}(\omega) + \sum_{k=1}^4 p(k) \sum_{j=2}^5 C_{j,e,b,m}^{(\text{el})}(k, a) \mathcal{F}_{j,k}^{(\text{el})}(\omega). \quad (6)$$

In the expression above $p(k) = 0.25$, $C_e^{(\text{vib,el})} = 2(|\mathcal{D}^{(\text{vib,el})}|^2)/3\hbar$, $C_b^{(\text{vib,el})} = 2(|\mathcal{M}^{(\text{vib,el})}|^2)/3\hbar$ and $C_m^{(\text{vib,el})} = 2i\langle \text{Im}[\mathcal{D}^{(\text{vib,el})} \cdot \mathcal{M}^{(\text{vib,el})}] \rangle / 3\hbar$, where $\langle (\dots) \rangle$ indicates the ensemble-average (calculated as time-average over the \approx ns MD time-scale in our ergodic assumption), $\mathcal{D}^{(\text{vib})} = \mathbf{d}^{01}$, $\mathcal{D}_j^{(\text{el})} = \mathbf{d}_{1j}$, $\mathcal{M}^{(\text{vib})} = \mathbf{m}^{01}$ and

$\mathcal{M}_j^{(\text{el})} = \mathbf{m}_{1j}$. The angular frequency dependence of the polarizabilities is accounted by $\mathcal{F}^{(\text{vib})}(\omega) = \sum_{\sigma=\pm 1} \sigma/(\omega + \sigma(\omega_v) + i\gamma_v/2)$ and $\mathcal{F}_{j,k}^{(\text{el})}(\omega) = \sum_{\sigma=\pm 1} \sigma/[\omega + \sigma(\omega_j(k) - \omega_1(k)) + i\gamma_j^{(\text{e})}(k)/2]$, where $\gamma_v = 0.012 \text{ fs}^{-1}$ is the relaxation rate of the only reparation vibrational transition $v = 0 \rightarrow 1$ with energy $\hbar\omega_v = 0.218 \text{ eV}$ (corresponding to the transition wavelength $\lambda = 5.69 \text{ }\mu\text{m}$). The calculated electric/magnetic transition dipole moments $\mathbf{d}^{01}, \mathbf{m}^{01}$ provide $\sqrt{\langle |\mathbf{d}^{01}|^2 \rangle}/d_0 = 0.105$, $\sqrt{\langle |\mathbf{m}^{01}|^2 \rangle}/m_0 = 0.398$ and $\langle \text{Im}[\mathbf{d}^{01}(\text{S}) \cdot \mathbf{d}^{01}(\text{S})] \rangle/d_0 m_0 = 0.007$, where $d_0 = |e|a_0$, $a_0 = \hbar/m_e c \alpha$ is the Bohr radius, $m_0 = |e|\hbar/2m_e$ is the Bohr magneton, α is the fine-structure constant and e, m_e are the electron charge and mass. The electronic relaxation rates $\gamma_j^{(\text{e})}$ have been extracted by the frequency bandwidth of the UV absorption spectrum and are reported in Table S1 along with the electronic transition energies, the electric/magnetic transition dipole moment moduli and the chiral projections expressed as ensemble averages. While in principle such a procedure might provide inconsistent results, we find that averaging over time the full microscopic polarizabilities (we calculate ensemble averages as time averages in our ergodic assumptions) or adopting individually averaged electric/magnetic transition dipole moduli, chiral projections and transition energies provides consistent results, see Fig. S1 for comparison.

In the limit of dilute drug solution, reparation dissolved in water can be treated as an effective-medium with bi-anisotropic macroscopic response by introducing the polarization $\mathbf{P}(\mathbf{r}, t) = \sum_{a=\text{R,S}} n_{\text{mol}}^{(a)} \langle \mathbf{d}_a(\mathbf{r}, t) \rangle$ and magnetization $\mathbf{M}(\mathbf{r}, t) = \sum_{a=\text{R,S}}$

$n_{\text{mol}}^{(a)} \langle \mathbf{m}_a(\mathbf{r}, t) \rangle$ fields. Such vectorial fields depend over the orientation-averaged^{31,32} electric/magnetic induced dipole moments $\langle \mathbf{d}_a \rangle, \langle \mathbf{m}_a \rangle$ and the number molecular densities $n_{\text{mol}}^{(\text{R,S})}$ of the two enantiomeric forms $a = \text{R,S}$. In turn, the macroscopic displacement vector $\mathbf{D}(\mathbf{r}, t) = \epsilon_0 \mathbf{E}(\mathbf{r}, t) + \mathbf{P}(\mathbf{r}, t)$ and magnetic field $\mathbf{H}(\mathbf{r}, t) = \mathbf{B}(\mathbf{r}, t)/\mu_0 - \mathbf{M}(\mathbf{r}, t)$ are given by the bi-anisotropic dispersion relations

$$\mathbf{D} = \epsilon_0 \text{Re} \left\{ [\epsilon_r(\lambda) \mathbf{E}_0(\mathbf{r}) - i\mu_0 c \kappa(\lambda) \mathbf{H}_0(\mathbf{r})] e^{-i\omega t} \right\}, \quad (7a)$$

$$\mathbf{B} = \mu_0 \text{Re} \left\{ \left[\frac{i\kappa(\lambda)}{\mu_0 c} \mathbf{E}_0(\mathbf{r}) + \mu_r(\lambda) \mathbf{H}_0(\mathbf{r}) \right] e^{-i\omega t} \right\}, \quad (7b)$$

where $\epsilon_r(\lambda) = \epsilon_{\text{H}_2\text{O}}(\lambda) + n_{\text{mol}} \alpha_e(\lambda)/\epsilon_0$ is the relative dielectric permittivity, $\kappa(\lambda) = i \sum_{a=\text{R,S}} n_{\text{mol}}^{(a)} \alpha_m^{(a)}(\lambda)/\epsilon_0 c$ is the chiral parameter and $\mu_r(\lambda) = 1 + \mu_0 n_{\text{mol}} \alpha_b(\lambda)$ is the relative magnetic permeability of the chiral mixture (see supplementary material, where we report a MATLAB script for the calculation of ϵ_r, μ_r and κ).

Because the mixing polarizability flips sign for opposite enantiomers, $\alpha_m^{(\text{R})} = -\alpha_m^{(\text{S})}$, the chiral parameter is proportional to the enantiomeric number density imbalance $\Delta n_{\text{mol}} = n_{\text{mol}}^{(\text{S})} - n_{\text{mol}}^{(\text{R})}$. Hence, optical activity vanishes for racemic mixtures where $n_{\text{mol}}^{(\text{R})} = n_{\text{mol}}^{(\text{S})}$. Note that $\epsilon_r(\lambda) = \epsilon_{\text{H}_2\text{O}}(\lambda) + \Delta\epsilon_r(\lambda)$ accounts for both the dielectric permittivity of the solvent (water) $\epsilon_{\text{H}_2\text{O}}(\lambda)$ ³⁷ and the calculated correction produced by reparation $\Delta\epsilon_r(\lambda)$. In Figs. 3(a)–3(f) we illustrate the dependence of $\Delta\epsilon_r(\lambda), \kappa(\lambda)$ and $\mu_r(\lambda)$ of a solution of pure S reparation enantiomers dissolved in water ($n_{\text{mol}}^{(\text{R})} = 0$) over the molecular number density n_{mol} and the

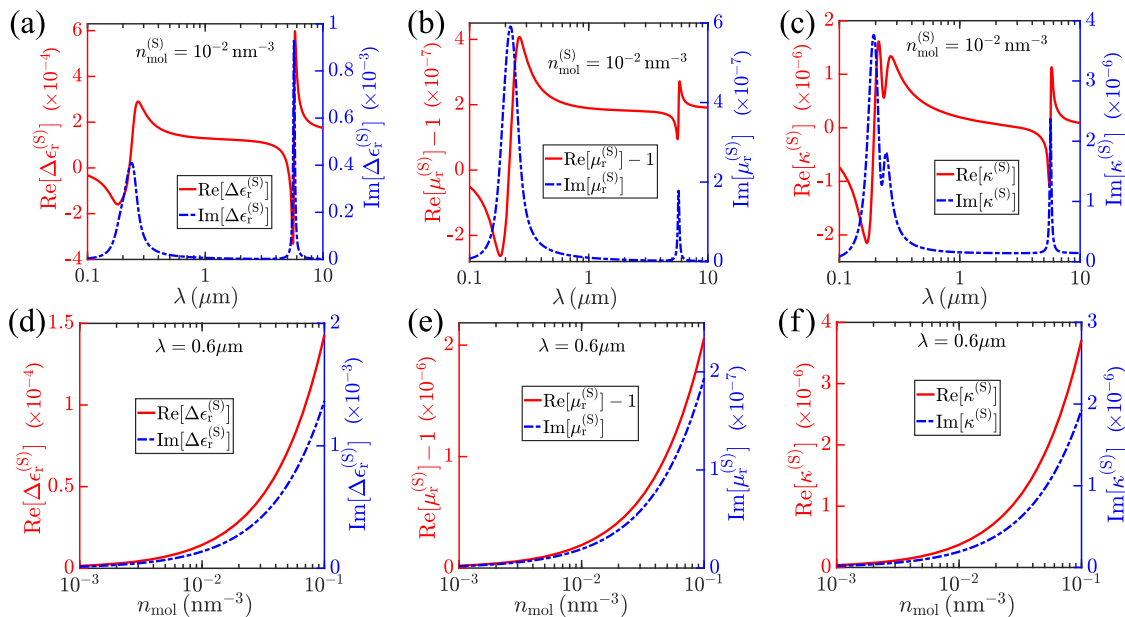


FIG. 3. (a)–(c) Vacuum wavelength λ and [(d)–(f)] number molecular density n_{mol} dependencies of [(a) and (d)] relative dielectric permittivity correction $\Delta\epsilon_r$, [(b) and (e)] relative magnetic permeability correction $\mu_r - 1$, and [(c) and (f)] chiral parameter κ of a water solution containing only the S enantiomer of reparation for [(a)–(c)] fixed molecular number density $n_{\text{mol}} = 10^{-2} \text{ nm}^{-3}$ and [(d)–(f)] fixed vacuum wavelength $\lambda = 600 \text{ nm}$.

vacuum wavelength of impinging radiation λ . Note that the chiroptical response of reparixin is affected by the tails of electronic (resonant at $\lambda \simeq 250$ nm) and vibrational transitions (resonant at $\lambda \simeq 6$ μm). The real part of $\epsilon_r(\lambda)$ is the leading contribution to the refractive index dispersion $n(\lambda) = \text{Re}[\sqrt{\epsilon_r(\lambda)}]$, which is dominated by the refractive index of water due to the dilute molecular number density $10^{-3} \text{ nm}^{-3} < n_{\text{mol}} < 10^{-1} \text{ nm}^{-3}$, see Figs. 3(a) and 3(d). The chirally insensitive extinction coefficient $k_{\text{ext}}(\lambda) = \text{Im}[\sqrt{\epsilon_r(\lambda)}]$ is affected mainly by the imaginary part of $\epsilon_r(\lambda)$ and is also dominated by the absorption of water, see Figs. 3(a) and 3(d). The relative magnetic permeability $\mu_r(\lambda)$ arises from the reparixin magnetic response but is chirally insensitive and provides only a tiny correction to the mixture absorption and dispersion, see Figs. 3(b) and 3(e). The dependence of the complex dimensionless chiral parameter $\kappa(\lambda)$ over vacuum wavelength λ and molecular number density n_{mol} is depicted in Figs. 3(c) and 3(f). Note that the chiral parameter is responsible for the rotatory power (proportional to $\text{Re}[\kappa(\lambda)]$) and CD (proportional to $\text{Im}[\kappa(\lambda)]$), and is maximised at the electronic/vibrational resonances of reparixin.

IV. PLASMON-ENHANCED CD SPECTROSCOPY

Figure 4(a) illustrates the considered Otto coupling scheme composed of a silica prism and a noble metal substrate separated by a distance d ($100 \text{ nm} < d < 1 \mu\text{m}$) embedding the chiral drug solution to be analysed, reparixin dissolved in water in our calculations. We consider monochromatic radiation with vacuum wavelength λ , incidence angle θ and arbitrary polarization given by the superposition of right ($s = +1$) and left ($s = -1$) circular components, impinging from a BK7 silica prism with relative dielectric permittivity $\epsilon_g(\lambda)$ ³⁸ ($z < 0$, see Fig. 4(a)) on a layer of reparixin dissolved in water [with bi-anisotropic response given by Eqs. (7a) and (7b)] placed at $0 < z < d$ and a metal substrate with dielectric constant $\epsilon_m(\lambda)$ in $z > d$. Because circular polarization waves are eigenfunctions of Maxwell's equations in the considered chiral medium, we decompose the impinging wave on circular polarization unit vectors $\hat{\mathbf{e}}_s^{(o)}(\theta) = (\cos \theta \hat{\mathbf{e}}_x + i s \hat{\mathbf{e}}_y - \sin \theta \hat{\mathbf{e}}_z)/\sqrt{2}$ and investigate the scattering

dynamics of circular polarization waves by analytically solving macroscopic Maxwell's equations accounting for the distinct polarization and magnetization fields in every medium of the considered geometry. We obtain

$$\mathbf{E}_o(\mathbf{r}, t) = \sum_{s=\pm 1} \text{Re} \left\{ \left[\mathbf{E}_z^{(o,s)}(\mathbf{r}) \Theta(-z) + \mathbf{E}_{\text{in}}^{(o,s)}(\mathbf{r}) \Theta_{\text{in}}(z) + \mathbf{E}_>^{(o,s)}(\mathbf{r}) \Theta(z-d) \right] e^{-i\omega t} \right\}, \quad (8)$$

$$\mathbf{H}_o(\mathbf{r}, t) = \sum_{s=\pm 1} \text{Re} \left\{ \frac{s}{i\mu_0 c} \left[\sqrt{\epsilon_g} \mathbf{E}_z^{(o,s)}(\mathbf{r}) \Theta(-z) + \frac{\sqrt{\epsilon_r}}{\sqrt{\mu_r}} \mathbf{E}_{\text{in}}^{(o,s)}(\mathbf{r}) \Theta_{\text{in}}(z) + \sqrt{\epsilon_m} \mathbf{E}_>^{(o,s)}(\mathbf{r}) \Theta(z-d) \right] e^{-i\omega t} \right\}, \quad (9)$$

where the subscript/superscript “o” indicates the considered Otto configuration, $\Theta(z)$ is the Heaviside step function, $\Theta_{\text{in}}(z) = \Theta(z) - \Theta(z-d)$,

$$\mathbf{E}_z^{(o,s)}(\mathbf{r}) = \left[E_{0,s}^{(o)} \hat{\mathbf{e}}_s^{(o)} e^{ik_g z} + E_{R,s}^{(o)} \hat{\mathbf{e}}_s^{(R)} e^{-ik_g z} \right] e^{ik_x x}, \quad (10a)$$

$$\mathbf{E}_{\text{in}}^{(o,s)}(\mathbf{r}) = \sum_{\sigma=\pm 1} E_{\sigma,s}^{(o)} \left[\sigma \hat{\mathbf{e}}_x - i \frac{k_0}{\beta_s} (\kappa - s \sqrt{\epsilon_r \mu_r}) \hat{\mathbf{e}}_y - \frac{k_x}{\beta_s} \hat{\mathbf{e}}_z \right] e^{ik_x x + i\sigma \beta_s z}, \quad (10b)$$

$$\mathbf{E}_>^{(o,s)}(\mathbf{r}) = \frac{1}{\sqrt{2}} E_{T,s}^{(o)} \left[\sqrt{1 - \frac{\epsilon_g}{\epsilon_m} \sin^2 \theta} \hat{\mathbf{e}}_x + i s \hat{\mathbf{e}}_y - \sqrt{\epsilon_g/\epsilon_m} \sin \theta \hat{\mathbf{e}}_z \right] e^{ik_x x + ik_m z}, \quad (10c)$$

$\omega = 2\pi c/\lambda$ is the angular frequency, $k_0 = \omega/c$, $E_{0,\pm 1}^{(o)}$ are the projections of the impinging vectorial amplitude over $\hat{\mathbf{e}}_{\pm 1}^{(o)}$, $\hat{\mathbf{e}}_s^{(R)} = (-\cos \theta \hat{\mathbf{e}}_x + i s \hat{\mathbf{e}}_y - \sin \theta \hat{\mathbf{e}}_z)/\sqrt{2}$, $k_x = k_0 \sqrt{\epsilon_g} \sin \theta$ is the conserved

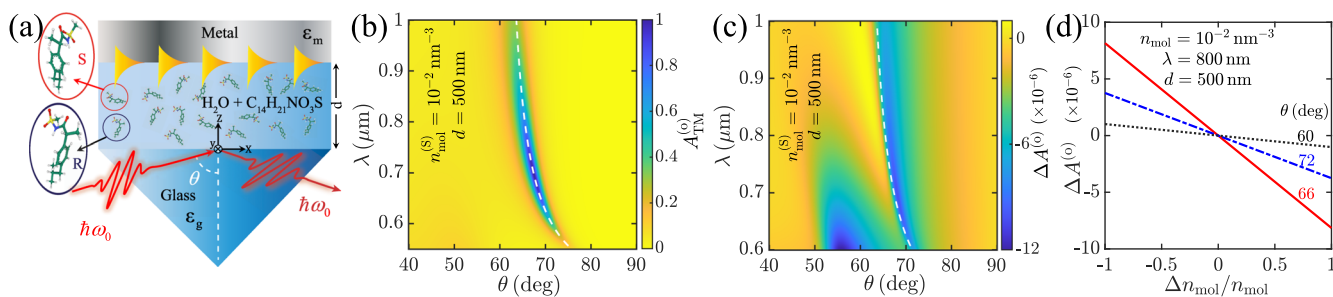


FIG. 4. (a) Schematic representation of plasmon-enhanced CD in the Otto configuration. The considered chiral sample is a solution of S and R reparixin enantiomers dissolved in water with molecular density n_{mol} . [(b) and (c)] Dependence of (b) TM absorbance $A_{\text{TM}}^{(o)}(\theta, \lambda)$ (for TM linear polarization excitation) and (c) CDDA $\Delta A^{(o)}(\theta, \lambda) = A_{\text{R}}(\theta, \lambda) - A_{\text{L}}(\theta, \lambda)$ (for circular polarization excitations) over the vacuum wavelength λ and the angle of incidence θ of the impinging radiation in the Otto coupling scheme illustrated in (a). The plots refer to a pure S reparixin enantiomer dissolved in water (with enantiomeric number density imbalance $\Delta n_{\text{mol}} = n_{\text{mol}}^{(S)} - n_{\text{mol}}^{(R)} = n_{\text{mol}}$). (d) Dependence of CDDA over the enantiomeric number density imbalance $\Delta n_{\text{mol}} = n_{\text{mol}}^{(S)} - n_{\text{mol}}^{(R)}$ for several distinct incidence angles θ and fixed excitation vacuum wavelength $\lambda = 800$ nm. All plots are obtained for a silver substrate with dielectric constant $\epsilon_m(\lambda)$ (taken from Ref. 39), fixed solvate aqueous reparixin thickness $d = 500$ nm and fixed total molecular number density $n_{\text{mol}} = 10^{-2} \text{ nm}^{-3}$. The dashed white curves in [(b) and (c)] indicate the SPP dispersion relation.

impinging \mathbf{k} -vector x -component, $\beta_s = \sqrt{k_0^2(\kappa - s\sqrt{\epsilon_r\mu_r})^2 - k_x^2}$ is the polarization-dependent wave-vector z -component leading to optical activity and $k_{g,m} = \sqrt{k_0^2\epsilon_{g,m} - k_x^2}$. In order to calculate the s -dependent forward ($\sigma = +1$) and backward ($\sigma = -1$) amplitudes within the chiral medium $E_{\sigma,s}^{(o)}$, the reflected ($E_{R,s}^{(o)}$) and transmitted ($E_{T,s}^{(o)}$) field amplitudes, we apply the boundary conditions (BCs) for the continuity of (i) the normal components of the displacement vector and induction magnetic field, and (ii) the tangential components of the electric and magnetic fields at the interfaces $z = 0, d$. Such BCs provide an 8×8 inhomogeneous system of algebraic equations for the field amplitudes, see Eq. (S1) in the supplementary material, which we invert numerically, obtaining $E_{R,\pm 1}^{(o)}, E_{T,\pm 1}^{(o)}$ for any impinging field components $E_{0,\pm 1}^{(o)}$. Note that, for racemic mixtures such that $n_{\text{mol}}^{(S)} = n_{\text{mol}}^{(R)}$ and $\kappa = 0$, electromagnetic excitations of the system, see Fig. 4(a), can be split into independent transverse magnetic (TM) and transverse electric (TE) components. Conversely, owing to the chirality of reparixin enantiomers, non-racemic mixtures such that $n_{\text{mol}}^{(S)} \neq n_{\text{mol}}^{(R)}$ produce mixed polarization dynamics. The absorbance of the system upon right ($s = +1, E_{0,-}^{(o)} = 0$) and left ($s = -1, E_{0,+}^{(o)} = 0$) circular polarization excitation is in turn given by $A_s^{(o)}(\theta, \lambda) = 1 - \sum_{\sigma=\pm 1} |E_{R,\sigma}^{(o)}|^2 / |E_{0,s}^{(o)}|^2$, from which we calculate the CDDA $\Delta A^{(o)}(\theta, \lambda) = A_+^{(o)} - A_-^{(o)}$. The TM absorbance $A_{\text{TM}}^{(o)}(\theta, \lambda) = 1 - \sum_{\sigma=\pm 1} |E_{R,\sigma}^{(o)}|^2 / |E_0|^2$ is obtained by calculating $E_{R,\sigma}^{(o)}$ for TM impinging polarization, i.e., $E_{0,+}^{(o)} = E_{0,-}^{(o)} = E_0$. In Fig. 4(b) we depict the dependence of $A_{\text{TM}}^{(o)}$ over λ, θ considering silver as a metal substrate. Note that the absorbance is maximised at the SPP excitation curve

$$\theta_{\text{SPP}}(\lambda) \simeq \arcsin \left\{ \text{Re} \sqrt{\frac{\epsilon_r(\lambda)\epsilon_m(\lambda)}{\epsilon_g(\lambda)[\epsilon_g(\lambda) + \epsilon_m(\lambda)]}} \right\}, \quad (11)$$

which is indicated by the white lines in Figs. 4(b) and 4(c). As a consequence of SPP resonant absorption CDDA is enhanced at the

SPP dispersion curve, see Fig. 4(c) where we plot $\Delta A^{(k)}$ as a function of λ, θ . For right/left circular polarization excitation, also a Fabry-Perot resonance is excited at $600 \text{ nm} < \lambda < 800 \text{ nm}$ and $50^\circ < \theta < 60^\circ$, which enhances CDDA by a factor $f_{\text{CDDA}} \simeq 10$.

V. DISCUSSION

Non-racemic mixtures such that $n_{\text{mol}}^{(S)} \neq n_{\text{mol}}^{(R)}$ produce mixed polarization dynamics analogously to optical rotation in bulk chiral media. The reflected radiation polarization can be fully tracked through the Stokes parameters $S_0^{(o)} = |E_{R,+}^{(o)}|^2 + |E_{R,-}^{(o)}|^2$, $S_1^{(o)} = 2\text{Re}[E_{R,+}^{(o)}E_{R,-}^{(o)*}]$, $S_2^{(o)} = -2\text{Im}[E_{R,+}^{(o)}E_{R,-}^{(o)*}]$, $S_3^{(o)} = |E_{R,+}^{(o)}|^2 - |E_{R,-}^{(o)}|^2$, whose dependence over the incidence angle θ is depicted in Figs. 5(a)–5(c) at $\lambda = 700 \text{ nm}$ for a silver substrate. At the SPP excitation angle $\theta_{\text{SPP}} \simeq 70^\circ$ polarization modulation is maximised for both circular and TM excitation polarization. Moreover, at $\theta \simeq 50^\circ$ polarization dynamics is also enhanced due to Fabry-Perot resonance of solvated reparixin. Such a phenomenon does not occur when the drug solution is probed in the Kretschmann coupling scheme, schematically depicted in Fig. 6(a). Here, analytical solutions of Maxwell's equations provide

$$\mathbf{E}_k(\mathbf{r}, t) = \sum_{s=\pm 1} \text{Re} \left\{ \left[\mathbf{E}_<^{(k,s)}(\mathbf{r})\Theta(-z) + \mathbf{E}_{\text{in}}^{(k,s)}(\mathbf{r})\Theta_{\text{in}}(z) + \mathbf{E}_>^{(k,s)}(\mathbf{r})\Theta(z-d) \right] e^{-i\omega t} \right\}, \quad (12)$$

$$\mathbf{H}_k(\mathbf{r}, t) = \sum_{s=\pm 1} \text{Re} \left\{ \frac{s}{i\mu_0 c} \left[\sqrt{\epsilon_g} \mathbf{E}_<^{(k,s)}(\mathbf{r})\Theta(-z) + \sqrt{\epsilon_m} \mathbf{E}_{\text{in}}^{(k,s)}(\mathbf{r})\Theta_{\text{in}}(z) + \frac{\sqrt{\epsilon_r}}{\sqrt{\mu_r}} \mathbf{E}_>^{(k,s)}(\mathbf{r})\Theta(z-d) \right] e^{-i\omega t} \right\}, \quad (13)$$

where

$$\mathbf{E}_<^{(k,s)}(\mathbf{r}) = \left[E_{0,s}^{(k)} \hat{\mathbf{e}}_s^{(o)} e^{ik_g z} + E_{R,s}^{(k)} \hat{\mathbf{e}}_s^{(R)} e^{-ik_g z} \right] e^{ik_x x}, \quad (14a)$$

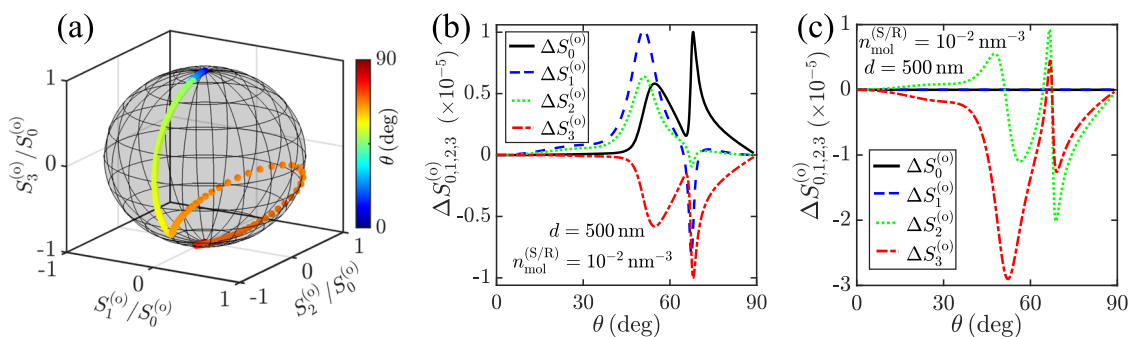


FIG. 5. Reflected polarization dynamics considering a silver substrate with dielectric constant $\epsilon_m(\lambda)$,³⁹ vacuum wavelength $\lambda = 700 \text{ nm}$, solvated aqueous reparixin with thickness $d = 500 \text{ nm}$ and total molecular number density $n_{\text{mol}} = 10^{-2} \text{ nm}^{-3}$. (a) Evolution of the Stokes parameters as a function of incidence angle θ in the Poincaré sphere for right-circular impinging polarization and pure S solvated aqueous reparixin with enantiomeric number density imbalance $\Delta n_{\text{mol}} = n_{\text{mol}}^{(S)} - n_{\text{mol}}^{(R)} = n_{\text{mol}}$. (b) and (c) Stokes parameters variation between pure S and pure R solvated aqueous reparixin upon (b) right-circular and (c) TM impinging polarization.

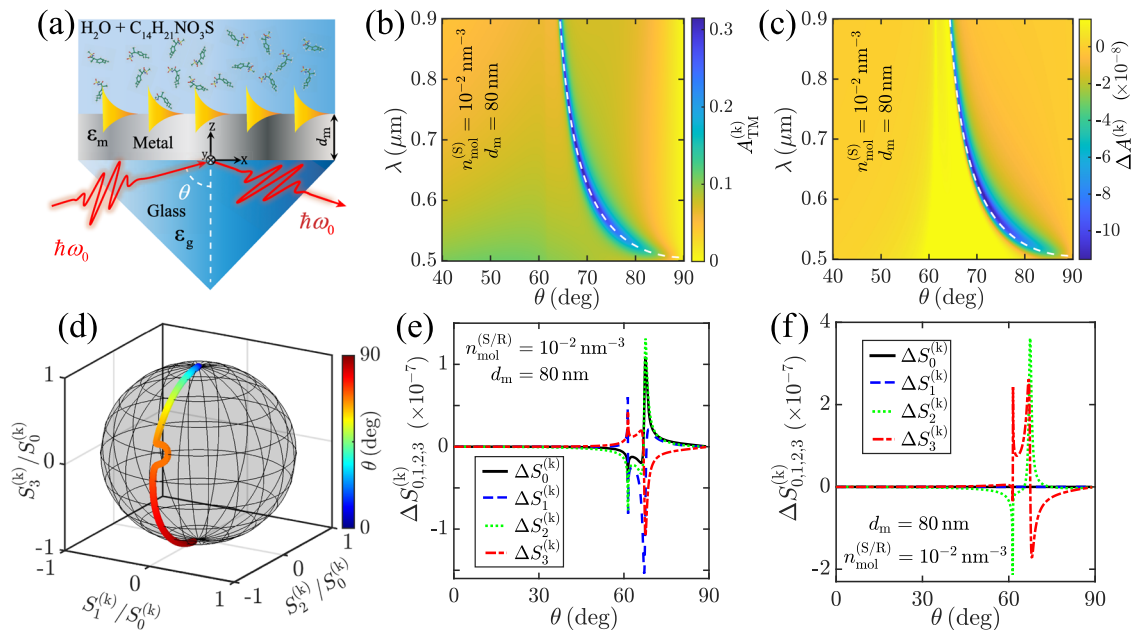


FIG. 6. (a) Schematic representation of plasmon-enhanced CD in the Kretschmann configuration. The considered chiral sample is a solution of S and R reparixin enantiomers dissolved in water with molecular density n_{mol} . (b) and (c) Dependence of (b) TM absorbance $A_{\text{TM}}(\theta, \lambda)$ and (c) CDDA $\Delta A(\theta, \lambda) = A_{\text{R}}(\theta, \lambda) - A_{\text{L}}(\theta, \lambda)$ (for circular polarization excitation) over the vacuum wavelength λ and angle of incidence θ of the impinging radiation. Both plots are obtained for a silver thin film with thickness $d_{\text{m}} = 80$ nm, dielectric constant $\epsilon_{\text{m}}(\lambda)$ (taken from Ref. 39) and a chiral medium with total molecular number density $n_{\text{mol}} = 10^{-2} \text{ nm}^{-3}$ and enantiomeric number density imbalance $\Delta n_{\text{mol}} = n_{\text{mol}}^{(\text{S})} - n_{\text{mol}}^{(\text{R})} = n_{\text{mol}}$. (d) Evolution of the Stokes parameters as a function of incidence angle θ in the Poincaré sphere for right-circular impinging polarization, pure S solvated aqueous reparixin with enantiomeric number density imbalance $\Delta n_{\text{mol}} = n_{\text{mol}}^{(\text{S})} - n_{\text{mol}}^{(\text{R})} = n_{\text{mol}}$ and impinging vacuum wavelength $\lambda = 700$ nm. (e) and (f) Stokes parameters variation between pure S and pure R solvated aqueous reparixin upon (e) right-circular and (f) TM impinging polarization for impinging vacuum wavelength $\lambda = 700$ nm.

$$\mathbf{E}_{\text{in}}^{(k,s)}(\mathbf{r}) = \sum_{\sigma=\pm 1} \frac{1}{\sqrt{2}} E_{\sigma,s}^{(k)} \left[\sigma \sqrt{1 - \frac{\epsilon_{\text{g}}}{\epsilon_{\text{m}}} \sin^2 \theta} \hat{\mathbf{e}}_x + i s \hat{\mathbf{e}}_y - \sqrt{\epsilon_{\text{g}}/\epsilon_{\text{m}}} \sin \theta \hat{\mathbf{e}}_z \right] e^{i k_x x + i \sigma k_m z}, \quad (14b)$$

$$\mathbf{E}_{>}^{(k,s)}(\mathbf{r}) = E_{\text{T},s}^{(k)} \left[\hat{\mathbf{e}}_x - i \frac{k_0}{\beta_s} (\kappa - s \sqrt{\epsilon_r \mu_r}) \hat{\mathbf{e}}_y - \frac{k_x}{\beta_s} \hat{\mathbf{e}}_z \right] e^{i k_x x + i \beta_s z}. \quad (14c)$$

Note that in the expressions above the roman subscript/superscript “k” indicates the considered Kretschmann configuration. Again, applying BCs one gets an 8×8 inhomogeneous system of algebraic equations for the field amplitudes, see Eq. (S10) in the supplementary material, which we invert numerically, obtaining $E_{\text{R},\pm 1}^{(k)}, E_{\text{T},\pm 1}^{(k)}$ for any impinging field components $E_{0,\pm 1}^{(k)}$. Hence, in the Kretschmann coupling scheme, the absorbance upon right ($s = +1, E_{0,-}^{(k)} = 0$) and left ($s = -1, E_{0,+}^{(k)} = 0$) circular polarization excitation is given by $A_s^{(k)}(\theta, \lambda) = 1 - \sum_{\sigma=\pm 1} |E_{\text{R},\sigma}^{(k)}|^2 / |E_{0,s}^{(k)}|^2$, from

which we calculate the Kretschmann CDDA $\Delta A^{(k)}(\theta, \lambda) = A_+^{(k)} - A_-^{(k)}$. Similarly to the Otto coupling scheme, the TM absorbance $A_{\text{TM}}^{(k)}(\theta, \lambda) = 1 - \sum_{\sigma=\pm 1} |E_{\text{R},\sigma}^{(k)}|^2 / |E_0|^2$ is obtained by calculating $E_{\text{R},\sigma}^{(k)}$ for TM impinging polarization, i.e., by setting $E_{0,+}^{(k)} = E_{0,-}^{(k)} = E_0$. In Figs. 6(b) and 6(c) we depict the dependence of (b) $A_{\text{TM}}^{(k)}$ and (c) $\Delta A^{(k)}$ over λ, θ considering a silver thin film with thickness $d_{\text{m}} = 80$ nm. Note that, similarly to the Otto coupling scheme, the TM absorbance and the CDDA are maximised at the SPP excitation curve $\theta_{\text{SPP}}(\lambda)$, indicated by the white lines in Figs. 6(b) and 6(c). Conversely to the Otto coupling scheme, Fabry-Perot resonances are not excited due to the intermediate metallic film. However, polarization dependent total internal reflection between glass and aqueous reparixin produces a CDDA absorption peak at $\theta \simeq 61^\circ$. It is worth emphasizing that such a phenomenon occurs only thanks to the sub-wavelength metallic thickness $d_{\text{m}} \ll \lambda$, enabling effective evanescent coupling between glass and aqueous reparixin. Also, note that the Kretschmann CDDA is about two orders of magnitude smaller than the Otto CDDA for identical total molecular number density n_{mol} and enantiomeric number density imbalance Δn_{mol} . We illustrate the dependence of the Kretschmann Stokes parameters ($S_0^{(k)} = |E_{\text{R},+}^{(k)}|^2 + |E_{\text{R},-}^{(k)}|^2, S_1^{(k)} = 2\text{Re}[E_{\text{R},+}^{(k)} E_{\text{R},-}^{(k)*}]$,

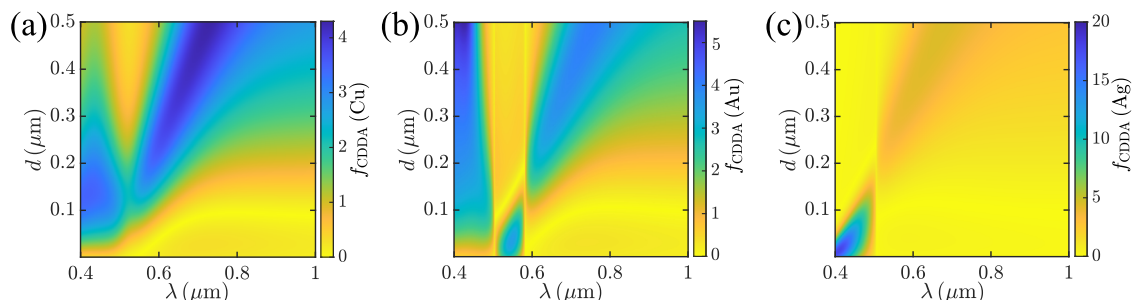


FIG. 7. Plasmon-induced CDDA enhancement factor $f_{\text{CDDA}}(\lambda) = \max_{\theta} |\Delta A^{(o,k)}| / |\Delta A_{\text{bulk}}|$ in the Otto coupling scheme for (a) copper, (b) gold and (c) silver substrates. The physical parameters used are identical to the ones used in Figs. 4(a) and 4(b), except the metal type included in ϵ_m , obtained from Ref. 39 for all the considered noble metals.

$S_2^{(k)} = -2\text{Im}[E_{R,+}^{(k)} E_{R,-}^{(o)*}]$, $S_3^{(k)} = |E_{R,+}^{(k)}|^2 - |E_{R,-}^{(k)}|^2$ over the incidence angle θ in Figs. 6(d)–6(f) at $\lambda = 700$ nm for a silver thin film with thickness $d_m = 80$ nm and a chiral medium with $n_{\text{mol}} = 10^{-2} \text{ nm}^{-3}$ and $\Delta n_{\text{mol}} = n_{\text{mol}}$. Again, note that the Stokes parameters modulation is much weaker in the Kretschmann coupling scheme, similarly to CDDA.

In order to quantify the plasmon-induced CDDA enhancement, we define the factor $f_{\text{CDDA}}(\lambda) = \max_{\theta} |\Delta A^{(o,k)}(\theta, \lambda)| / |\Delta A_{\text{bulk}}(\lambda)|$, where $\Delta A_{\text{bulk}}(\lambda) = e^{-2\text{Im}\beta_{\pm}^{(b)} d} - e^{-2\text{Im}\beta_{\pm}^{(o)} d}$ is the absorbance of a layer of reparixin dissolved in water in the absence of the nanophotonic structure and $\beta_{\pm}^{(b)} = k_0(\sqrt{\epsilon_r \mu_r} \mp \kappa)$. In Figs. 7(a)–7(c) we depict the vacuum wavelength dependence of the CDDA enhancement for silver, gold and copper interfaces in the Otto coupling scheme. Note that the maximum plasmon-induced CDDA enhancement $f_{\text{CDDA}} \approx 20$ is attained in the Otto configuration at $\lambda \approx 400$ nm adopting silver as metal substrate, see Fig. 7(c). However, for $\lambda > 500$ nm, gold and copper provide CDDA enhancement factors $f_{\text{CDDA}} \approx 5$ comparable with silver. We emphasize that, by assuming metal substrate lateral dimensions of the order of $1 \times 1 \text{ mm}^2$, the considered chiroptical interaction volume is $V_{\text{int}} \lesssim 1 \text{ nl}$ and the observed $\approx 10^{-6}$ CDDA can be readily measured using lock-in amplifiers. For the considered dilute molecular number density $n_{\text{mol}} \approx 10^{-2} \text{ nm}^{-3}$, we find that plasmon-enhanced CD spectroscopy is a viable chiroptical sensing platform able to discern $\lesssim 10^{13}$ R, S enantiomers in the considered V_{int} . We note that, in the considered Otto and Kretschmann coupling schemes, the transmitted intensity vanishes due to absorption because we assumed infinitely extended metal/chiral-sample for $z > d, d_m$. However, in practical experimental realizations, the physical dimensions of the metal/chiral-sample is finite and the transmitted intensity is non-vanishing. In turn, experimentally, absorbance can be measured as $A = 1 - I_R/I_0 - I_T/I_0$, where $I_{R,T,0}$ indicate the measured reflected (I_R), transmitted (I_T), and impinging (I_0) intensities. CDDA can be in turn measured as the absorbance difference upon left/right impinging polarization. The dissymmetry factor can be measured as the CDDA divided by the averaged absorbance upon left and right impinging polarization. We emphasize that, while the CDDA is enhanced due to SPP excitation, the dissymmetry factor remains unaffected by the nanostructure. Indeed, the role played by SPPs lies in the enhancement of the local electric field enabling both higher averaged absorbance and

higher CDDA, while maintaining their ratio (dissymmetry factor) unaffected. In turn, the proposed CD spectroscopic schemes are distinct from superchirality approaches^{12–16} aiming at enhancing the dissymmetry factor. Nevertheless, importantly the enhanced CDDA enables reducing the volume of the drug solution to be analysed, as illustrated above.

VI. CONCLUSIONS

We have investigated the potential of SPPs at interfaces between noble metals and a water solution of reparixin for plasmon-enhanced CD spectroscopy. The considered drug solution is composed of a realistic molecule adopted in clinical studies for patients with community-acquired pneumonia, including COVID-19 and acute respiratory distress syndrome. Our calculations of reparixin microscopic observables are based on MD simulations, TD-DFT and PMM simulations enabling the evaluation of time-averaged permanent and transition electric/magnetic dipole moments. Macroscopic optical parameters of the isotropic chiral mixture are calculated by perturbatively solving the density matrix equations. Our results indicate that SPP excitation enables plasmon-induced CDDA enhancement of the order $f_{\text{CDDA}} \approx 20$ of solutions with sub-nl volume. Our results are relevant for the development of innovative integrated schemes for chiroptical sensing of drug solutions.

SUPPLEMENTARY MATERIAL

See the supplementary material for the theoretical details on the reparixin quantum observables calculations, the system of algebraic equations for field amplitudes in the Otto and Kretschmann configurations, and a MATLAB script for the calculation of the macroscopic bi-anisotropic response of reparixin dissolved in water.

ACKNOWLEDGMENTS

This work has been partially funded by the European Union - NextGenerationEU under the Italian Ministry of University and Research (MUR) National Innovation Ecosystem Grant No. ECS00000041 - VITALITY - CUP E13C22001060006, the Progetti di

ricerca di Rilevante Interesse Nazionale (PRIN) of the Italian Ministry of Research PHOTO (PHOTonics Terahertz devices based on topological materials) Grant No. 2020RPEPNH, and the European Union under Grant Agreement No. 101046424. Views and opinions expressed are however those of the author(s) only and do not necessarily reflect those of the European Union or the European Innovation Council. Neither the European Union nor the European Innovation Council can be held responsible for them.

The authors acknowledge fruitful discussions with Jens Biegert, Patrice Genevet, Michele Dipalo, Giovanni Melle, Sotirios Christodoulou, Anna Maria Cimini, and Domenico Bonanni.

AUTHOR DECLARATIONS

Conflict of Interest

The authors have no conflicts to disclose.

Author Contributions

Matteo Venturi: Data curation (equal); Formal analysis (equal); Investigation (equal); Methodology (equal); Software (equal); Visualization (equal); Writing – original draft (equal); Writing – review & editing (equal). **Raju Adhikary:** Data curation (equal); Formal analysis (equal); Investigation (equal); Methodology (supporting); Software (supporting); Visualization (supporting); Writing – original draft (supporting); Writing – review & editing (equal). **Ambareesh Sahoo:** Data curation (supporting); Formal analysis (equal); Investigation (equal); Methodology (supporting); Software (supporting); Visualization (lead); Writing – original draft (supporting); Writing – review & editing (equal). **Carino Ferrante:** Investigation (supporting); Methodology (supporting); Project administration (supporting); Supervision (supporting); Visualization (supporting); Writing – original draft (supporting); Writing – review & editing (equal). **Isabella Daidone:** Formal analysis (supporting); Investigation (supporting); Methodology (supporting); Resources (supporting); Software (supporting); Supervision (supporting); Writing – original draft (supporting); Writing – review & editing (equal). **Francesco Di Stasio:** Conceptualization (supporting); Funding acquisition (equal); Project administration (supporting); Writing – review & editing (equal). **Andrea Toma:** Conceptualization (supporting); Funding acquisition (equal); Project administration (supporting); Writing – review & editing (equal). **Francesco Tani:** Conceptualization (supporting); Funding acquisition (equal); Project administration (supporting); Writing – review & editing (equal). **Hatice Altug:** Conceptualization (supporting); Funding acquisition (equal); Project administration (supporting); Writing – review & editing (equal). **Antonio Mecozzi:** Formal analysis (supporting); Investigation (supporting); Methodology (supporting); Writing – review & editing (equal). **Massimiliano Aschi:** Data curation (supporting); Formal analysis (supporting); Investigation (supporting); Methodology (equal); Resources (lead); Software (lead); Supervision (equal); Writing – original draft (supporting); Writing – review & editing (equal). **Andrea Marini:** Conceptualization (lead); Formal analysis (equal); Funding acquisition (equal); Investigation (equal); Methodology (equal); Project administration

(equal); Software (equal); Supervision (equal); Visualization (equal); Writing – original draft (equal); Writing – review & editing (equal).

DATA AVAILABILITY

The data that support the findings of this study are available within the article and its supplementary material.

REFERENCES

- ¹L. A. Nguyen, H. He, and C. Pham-Huy, “Chiral drugs: An overview,” *Int. J. Biomed. Sci.* **2**, 85–100 (2006).
- ²A. Shundo, J. Labuta, J. P. Hill, S. Ishihara, and K. Ariga, “Nuclear magnetic resonance signaling of molecular chiral information using an achiral reagent,” *J. Am. Chem. Soc.* **131**, 9494–9495 (2009).
- ³K. Manoli, M. Magliulo, and L. Torsi, “Chiral sensor devices for differentiation of enantiomers,” *Top. Curr. Chem.* **341**, 133–176 (2013).
- ⁴Y. Okamoto and T. Ikai, “Chiral HPLC for efficient resolution of enantiomers,” *Chem. Soc. Rev.* **37**, 2593–2608 (2008).
- ⁵T. Müller, K. B. Wiberg, and P. H. Vaccaro, “Cavity ring-down polarimetry (CRDP): A new scheme for probing circular birefringence and circular dichroism in the gas phase,” *J. Phys. Chem. A* **104**, 5959–5968 (2000).
- ⁶P. J. Stephens and M. A. Lowe, “Vibrational circular dichroism,” *Annu. Rev. Phys. Chem.* **36**, 213–241 (1985).
- ⁷S. S. Wesolowski and D. E. Pivonka, “A rapid alternative to X-ray crystallography for chiral determination: Case studies of vibrational circular dichroism (VCD) to advance drug discovery projects,” *Bioorg. Med. Chem. Lett.* **23**, 4019–4025 (2013).
- ⁸S. Beaulieu, A. Comby, D. Descamps, B. Fabre, G. A. Garcia, R. Géneaux, A. G. Harvey, F. Légaré, Z. Masin, L. Nahon, A. F. Ordonez, S. Petit, B. Pons, Y. Mairesse, O. Smirnova, and V. Blanchet, “Photoexcitation circular dichroism in chiral molecules,” *Nat. Phys.* **14**, 484–489 (2018).
- ⁹O. Neufeld, D. Ayuso, P. Decleva, M. Y. Ivanov, O. Smirnova, and O. Cohen, “Ultrasensitive chiral spectroscopy by dynamical symmetry breaking in high harmonic generation,” *Phys. Rev. X* **9**, 031002 (2019).
- ¹⁰D. Ayuso, O. Neufeld, A. F. Ordonez, P. Decleva, G. Lerner, O. Cohen, M. Y. Ivanov, and O. Smirnova, “Synthetic chiral light for efficient control of chiral light-matter interaction,” *Nat. Photonics* **13**, 866–871 (2019).
- ¹¹D. Ayuso, A. F. Ordonez, and O. Smirnova, “Ultrafast chirality: The road to efficient chiral measurements,” *Phys. Chem. Chem. Phys.* **24**, 26962–26991 (2022).
- ¹²Y. Tang and A. E. Cohen, “Optical chirality and its interaction with matter,” *Phys. Rev. Lett.* **104**, 163901 (2010).
- ¹³Y. Tang and A. E. Cohen, “Enhanced enantioselectivity in excitation of chiral molecules by superchiral light,” *Science* **332**, 333–336 (2011).
- ¹⁴E. Mohammadi, K. L. Tsakmakidis, A. N. Askarpour, P. Dehkhoda, A. Tavakoli, and H. Altug, “Nanophotonic platforms for enhanced chiral sensing,” *ACS Photonics* **5**, 2669–2675 (2018).
- ¹⁵G. Pellegrini, M. Finazzi, M. Celebrano, L. Duó, and P. Biagioni, “Surface-enhanced chiroptical spectroscopy with superchiral surface waves,” *Chirality* **30**, 883–889 (2018).
- ¹⁶C. Gilroy, S. Hashiyada, K. Endo, A. S. Karimullah, L. D. Barron, H. Okamoto, Y. Togawa, and M. Kadodwala, “Roles of superchirality and interference in chiral plasmonic biodetection,” *J. Phys. Chem. C* **123**, 15195–15203 (2019).
- ¹⁷E. Mohammadi, A. Tavakoli, P. Dehkhoda, Y. Jahani, K. L. Tsakmakidis, A. Tittl, and H. Altug, “Accessible superchiral near-fields driven by tailored electric and magnetic resonances in all-dielectric nanostructures,” *ACS Photonics* **6**, 1939–1946 (2019).
- ¹⁸E. Mohammadi, A. Tittl, K. L. Tsakmakidis, T. V. Raziman, and A. G. Curto, “Dual nanoresonators for ultrasensitive chiral detection,” *ACS Photonics* **8**, 1754–1762 (2021).
- ¹⁹M. L. Nesterov, X. Yin, M. Schaferling, H. Giessen, and T. Weiss, “The role of plasmon-generated near fields for enhanced circular dichroism spectroscopy,” *ACS Photonics* **3**, 578–583 (2016).

- ²⁰A. O. Govorov, "Plasmon-induced circular dichroism of a chiral molecule in the vicinity of metal nanocrystals. Application to various geometries," *J. Phys. Chem. C* **115**, 7914–7923 (2011).
- ²¹Z. Fan and A. O. Govorov, "Plasmonic circular dichroism of chiral metal nanoparticle assemblies," *Nano Lett.* **10**, 2580–2587 (2010).
- ²²J. M. Slocik, A. O. Govorov, and R. R. Naik, "Plasmonic circular dichroism of peptide-functionalized gold nanoparticles," *Nano Lett.* **11**, 701–705 (2011).
- ²³Z. Hu, D. Meng, F. Lin, X. Zhu, Z. Fang, and X. Wu, "Plasmonic circular dichroism of gold nanoparticle based nanostructures," *Adv. Opt. Mater.* **7**, 1801590 (2019).
- ²⁴A. Gorio, L. Madaschi, G. Zadra, G. Marfia, B. Cavalieri, R. Bertini, and A. M. Di Giulio, "Reparixin, an inhibitor of CXCR2 function, attenuates inflammatory responses and promotes recovery of function after traumatic lesion to the spinal cord," *J. Pharmacol. Exp. Ther.* **322**, 973–981 (2007).
- ²⁵G. Landoni, L. Piemonti, A. d'Arminio Monforte, P. Grossi, A. Zangrillo, E. Bucci, M. Allegretti, G. Goisis, E. M. Gavioli, N. Patel, M. De Pizzol, G. Pasedis, and F. Mantelli, "A multicenter phase 2 randomized controlled study on the efficacy and safety of reparixin in the treatment of hospitalized patients with COVID-19 pneumonia," *Infect. Dis. Ther.* **11**, 1559–1574 (2022).
- ²⁶S. Park, G. Lee, S. H. Song, C. H. Oh, and P. S. Kim, "Resonant coupling of surface plasmons to radiation modes by use of dielectric gratings," *Opt. Lett.* **28**, 1870 (2003).
- ²⁷H. L. Offerhaus, B. Van den Bergen, M. Escalante, F. B. Segerink, J. P. Korterik, and N. F. Van Hulst, "Creating focused plasmons by noncollinear phase-matching on functional gratings," *Nano Lett.* **5**, 2144–2148 (2005).
- ²⁸E. Kretschmann and H. Raether, "Notizen: Radiative decay of non radiative surface plasmons excited by light," *Z. Naturforsch. A* **23**, 2135 (1968).
- ²⁹A. Otto, "Excitation of nonradiative surface plasma waves in silver by the method of frustrated total reflection," *Z. Phys. A* **216**, 398 (1968).
- ³⁰I. R. Hooper and J. R. Sambles, "Coupled surface plasmon polaritons on thin metal slabs corrugated on both surfaces," *Phys. Rev. B* **70**, 045421 (2004).
- ³¹S. S. Andrews, "Using rotational averaging to calculate the bulk response of isotropic and anisotropic samples from molecular parameters," *J. Chem. Educ.* **81**, 877–885 (2004).
- ³²L. Ohnoutek, J.-Y. Kim, J. Lu, B. J. Olohan, D. M. Rășădean, G. Dan Pantoș, N. A. Kotov, and V. K. Valev, "Third-harmonic Mie scattering from semiconductor nanohelices," *Nat. Photonics* **16**, 126–133 (2022).
- ³³M. Aschi, R. Spezia, A. Di Nola, and A. Amadei, "A first-principles method to model perturbed electronic wavefunctions: The effect of an external homogeneous electric field," *Chem. Phys. Lett.* **344**, 374–380 (2001).
- ³⁴A. Amadei, M. D'Alessandro, M. D'Abramo, and M. Aschi, "Theoretical characterization of electronic states in interacting chemical systems," *J. Chem. Phys.* **130**, 084109 (2009).
- ³⁵O. Carrillo-Parramon, S. Del Galdo, M. Aschi, G. Mancini, A. Amadei, and V. Barone, "Flexible and comprehensive implementation of MD-PMM approach in a general and robust code," *J. Chem. Theory Comput.* **13**, 5506–5514 (2017).
- ³⁶A. O. Govorov and Z. Fan, "Theory of chiral plasmonic nanostructures comprising metal nanocrystals and chiral molecular media," *ChemPhysChem* **13**, 2551–2560 (2012).
- ³⁷G. M. Hale and M. R. Querry, "Optical constants of water in the 200-nm to 200- μ m wavelength region," *Appl. Opt.* **12**, 555–563 (1973).
- ³⁸See https://refractiveindex.info/download/data/2017/schott_2017-01-20.pdf for "Optical Glass Data Sheets."
- ³⁹B. Ung and Y. Sheng, "Interference of surface waves in a metallic nanoslit," *Opt. Express* **15**, 1182–1190 (2007).